*Research Article*

# Dynamic Drag Reduction Effects of Aerospikes and Aerodisks

**Rong Han [iD],[1] Wei Liu [iD],[1] Xiaoliang Yang [iD],[1] and Xinghua Chang[2]**

[1]*College of Aerospace Science and Engineering, National University of Defense Technology, Changsha, Hunan 410073, China*
[2]*Unmanned Systems Research Center, National Innovation Institute of Defense Technology, Beijing 100071, China*

Correspondence should be addressed to Wei Liu; fishfather6525@sina.com

In order to investigate the dynamic characteristics of blunt aircraft mounted with aerospikes and aerodisks in large-amplitude force-pitching, the Roe spatial scheme and the lower-upper symmetric Gauss-Seidel (LU-SGS) method with dual time step are employed for discretization of unsteady Navier-Stokes (N-S) equations. A parametric investigation on the flow fields is conducted by altering the pitching period, aerospike length, and aerodisk diameter consequently via a variable-controlling procedure. Dynamic characteristics of aerodynamic drag as well as the visualization of unsteady flow fields are achieved, and the results show that the aerodynamics of hypersonic aircraft under the condition of large-amplitude force-pitching vibration have hysteresis characteristics affected by periods of force-pitching vibration. In addition, when changing aerospike length and aerodisk diameter, the variation tendency of drag reduction efficiency is determined by the pitching angle of the oscillation process.

## 1. Introduction

When flying at hypersonic speed, aircrafts face problems of excessive drag and severe aerodynamic heating, which greatly reduce the payload of the aircraft [1]. These issues, also posing hidden dangers for the design and flight safety of hypersonic aircraft, address great scientific value and engineering significance to study the mechanism of drag reduction in this context.

Researches on blunt body drag reduction methods in hypersonic flows have mainly focused on the forward-facing cavity, the energy deposition, an opposing jet issued at the stagnation point, aerospikes, and additionally, their combinatorial configurations [2]. An aerospike protruding from the blunt body nose can push the strong bow shock away from the wall surface effectively and replace it with a weak conical one. At the same time, a recirculation region forms on both sides of the aerospike, which contributes to a comprehensive effect of drag reduction and heat protection. Due to its simplicity and effectiveness, the aerospike system was applied to the head of the Trident I missile by the Lockheed Martin Corporation (America) and was found to reduce drag by as much as 52% in hypersonic flows [3].

The first application of aerospikes to high-speed aircraft was by Alexander [4] of the Langley Pilotless Aircraft Research Division in 1947. Piland and Putland [5] introduced the term "spike," and it was quickly adopted. A large number of wind tunnel tests have been done since the early 1950s. In the early stages, researchers mostly focused on the flow-field reconstruction effect of aerospikes. Mair [6] found that the location of separation flow was related to aerospike length. When the length was greater than 1.5 times the blunt body diameter, the flow field displayed regular oscillation. Wood [7] conducted a wind-tunnel test on a cone-cylinder configuration with an aerospike in a Mach 10.0 flow and established a semi-empirical formula for the separation phenomenon. In addition, he defined five different flow states according to the aerospike length and cone angle. Menezes et al. [8] discovered that the circumfluence area was the critical factor which could affect the drag characteristics of aircraft. Moreover, he found unsteady oscillation phenomena in the flow field.

In the field of hypersonic passive drag reduction, scholars have attached great importance to the investigations of relevant parameters and performance. Substantial studies have also been carried out on different aerospike shapes [5, 9, 10]. Crawford [10] investigated the geometry with
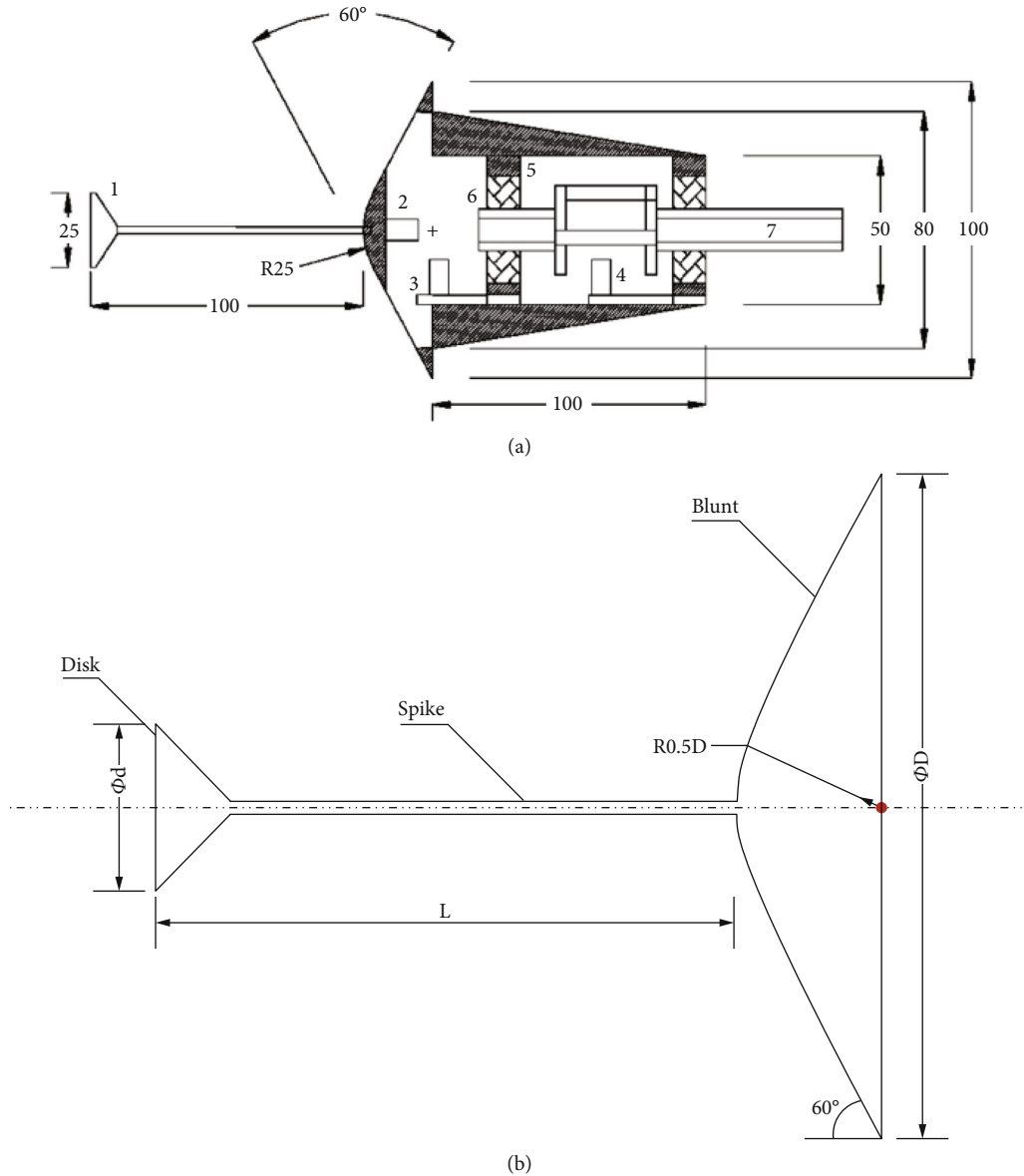
(a)

(b)

Figure 1: Experimental and numerical models of the aircraft with aerospike. (a) Experimental model. (b) Numerical simulation model.

different lengths under a Mach 6.8 flow, concluding that the pressure drag descended at first and then rose with increased aerospike length. Thurman [11] experimentally studied an arrangement with a deflection angle between the aerospike and the axis of the blunt body and realized that it could increase the lift-to-drag ratio. Gnemmi et al. [12] pointed out that the drag reduction rate of disk-spike, sphere-spike, and biological-spike configurations decreased gradually as the attack angle went up, until 15, 19, and 21 deg, respectively. After this inflection point, the drag reduction rate remained stable. Kalimuthu et al. [13] adopted a hemispherical-cylindrical shape and came to the conclusion that mounting the aerodisk in front of the aerospike reduced drag more significantly. Jiang et al. [14] considered cases in the low-pitching-angle region, and they found that the longer the aerospike and the larger the aerodisk, the more effective drag reduction was witnessed. However, as the aerospike

length and aerodisk radius changed, the drag reduction effect became saturated. Besides, the experimental data of Menezes et al. [8] and Crawford [10] are widely used for numerical validation.

In addition to the above experimental investigations, the rapid development of computer technology has enabled quite a few relevant numerical studies since the 1980s. These simulation results have deepened the understanding of flow fields around blunt aircraft with aerospikes and have a high instructive value in aerospike selection and optimization. Zhang and Huang [3] introduced the NND scheme to calculate N-S equations while analysing the formation and development of shocks and vortexes. Results showed that vortex bifurcation, merging, and secondary separation occurred in the separation region. Yamauchi et al. [15] identified the fact that aerospike length affected the area of the recirculation region in the head and then affected the pressure distribution on the wall surface,

resulting in a change in the aircraft drag coefficient. However, the Mach number of incoming flow had little effect on the size of the separation zone. Gerdroodbary and Hosseinalipour [16] carried out some three-dimensional numerical investigations on four aerospike configurations and arrived at the conclusion that a small conical shock angle led to direct impingement of the wall surface. Thus, the drag reduction rates of cut-shape and sharp-shape configurations were low. However, aerodisks and hemispheres did not face above problems. The influence of attack angle ($\alpha = 0°$, $2°$, $5°$, and $8°$) on the blunt drag coefficient was analysed by Sebastian et al. [17] in detail. Numerical results indicated that the drag reduction effect would be impaired as the angle of attack increased. The drag reduction efficiency could reach up to 77.014% at zero angle of attack. Kharati-Koopaee and Gazor [18] discussed the impact of aerodisk diameter and aerospike length. They recognized that with the increase of aerodisk diameter, the drag coefficient would decrease first and then rise. When the disc diameter was small, the drag coefficient maintained a descending tendency as aerospike length went up, and vice versa. Narayan et al. [19] carried out a comparison of different blunt ratios and semivertex angles and concluded that the shock detachment distance was linearly correlated to the bluntness ratio. In addition, when the blunt ratio and semivertex angle became small, the drag coefficient would follow suit. The numerical results of Zhao et al. [20] showed that Mach number had no effect on the drag reduction mechanism. However, the drag at the nose of the aerodisk increased as the Mach number rose.

These studies mentioned above mainly considered blunt aircraft with aerospikes in a static state. However, with the development of aviation and aerospace technology, high-attack angles and high-speed flights have become increasingly ubiquitous, accompanied by many complicated aerodynamic problems. When a blunt aircraft maneuvers at a high angle of attack, shock wave interaction, boundary layer separation, and other complex flow phenomena occur, and the flow around the blunt body is in a highly unsteady state. Low-amplitude forced-pitching oscillation of a blunt body in hypersonic flow is the standard model for dynamic experiments and has produced many experimental and engineering calculation results [21–23]. As for aircrafts installed with aerospikes and aerodisks, there are few studies regarding their dynamic characteristics. However, the drag reduction effect during the dynamic process must be different from that in the steady state. Therefore, it is of great significance with regard to hypersonic flights to investigate the unsteady flow field and aerodynamic characteristics exhibited by aircraft while executing dynamic motion. The findings would be useful in shape selection and control method design. In this paper, we consider the dynamic characteristics of blunt aircraft with aerospikes and aerodisks under large-amplitude oscillation. The unsteady flow fields are numerically simulated while changing the oscillation period, aerospike length, and aerodisk diameter. In addition, we analyse the drag reduction performance of the aerospike-disc configuration under large-amplitude forced oscillation in detail.

The paper is organized according to the following structure. In the second section, the physical model, numerical method, and meshing situation used in the numerical simulation are introduced. The accuracy of the numerical method used in this paper is verified by comparing it with the experimental results of Menezes et al. [8]. In Section 3.1, we analyse the flow field around the blunt vehicle with an aerodisk during the half period of a pitching oscillation. Then, we put an eye on the effect of pitching oscillation period on the drag characteristics of the aircraft. In Section 3.2 and Section 3.3, we adopt the variable-controlling method to study the effects of aerospike length and aerodisk diameter, respectively,

TABLE 1: Setup of the oscillation period, aerospike length, and aerodisk diameter. $D$ represents the base diameter of the blunt body.

| Parameter | Pitching-oscillation period ($T$) | Aerospike length/blunt diameter ($L/D$) | Aerodisk diameter/blunt diameter ($d/D$) |
|---|---|---|---|
| 1-1 | 62.5 | 1.0 | 0.3125 |
| 1-2 | 62.5 | 0.0 | 0.0 |
| 1-3 | 125 | 1.0 | 0.25 |
| 1-4 | 125 | 0.0 | 0.0 |
| 1-5 | 250 | 1.0 | 0.25 |
| 1-6 | 250 | 0.0 | 0.0 |
| 2-1 | 125 | 0.0 | 0.0 |
| 2-2 | 125 | 0.5 | 0.25 |
| 2-3 | 125 | 1.0 | 0.25 |
| 2-4 | 125 | 1.5 | 0.25 |
| 2-5 | 125 | 2.0 | 0.25 |
| 3-1 | 125 | 0.0 | 0.0 |
| 3-2 | 125 | 1.0 | 0.125 |
| 3-3 | 125 | 1.0 | 0.1875 |
| 3-4 | 125 | 1.0 | 0.25 |
| 3-5 | 125 | 1.0 | 0.3125 |
| 3-6 | 125 | 1.0 | 0.375 |

TABLE 2: Inflow conditions of the experiment.

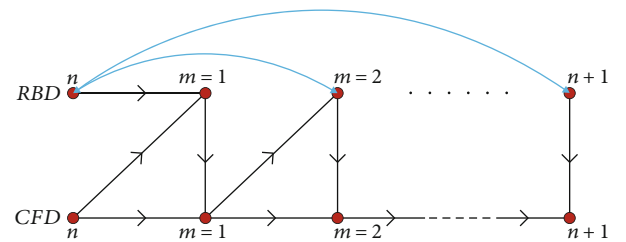| Variable | Value |
|---|---|
| $\rho_\infty$ (kg/m$^3$) | 0.0106 |
| $v_\infty$ (m/s) | 1363.36 |
| $\mu_\infty$ (kg/m•s) | $0.964 \times 10^{-5}$ |
| $P_0$ (Pa) | 425 |



FIGURE 2: Data interaction scheme of the strong coupling method. CFD (computational fluid dynamics) represents the solution of the Navier-Stokes equation, while RBD (rigid body dynamics) denotes the computation of flight dynamics and kinematics equations.
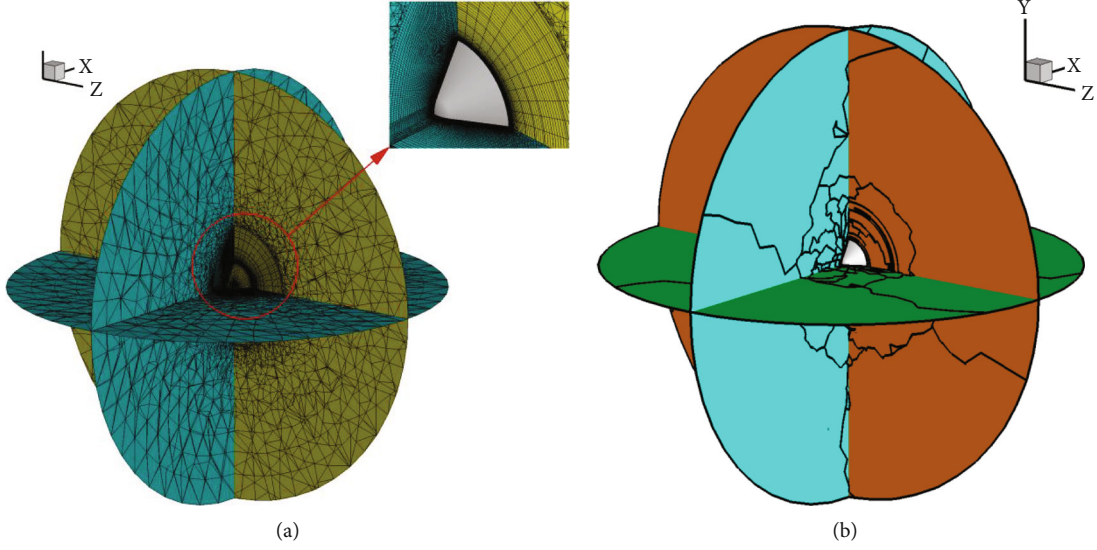
(a)

(b)

FIGURE 3: Schematic diagram of grid generation and partition. (a) Three-dimensional grid. (b) Grid partition.

especially on drag characteristics of the aircraft during pitching oscillation. Finally, we summarize and expound the conclusions in the fourth section.

## 2. Numerical Method

*2.1. Physical Model.* Menezes et al. [8] compared the effects of different aerospikes in reducing drag and aerodynamic heating. The geometric model for their experiment is shown in Figure 1(a) and is widely used to verify the accuracy of numerical methods. They measured the drag coefficient Cd of a large-angle blunt body in hypersonic flow (results are given in Ref. 8). The physical model for our study is a simplified version of this geometry (see Figure 1(b)). The apex angle of the blunt head is 120 deg. The aerospike extended from the blunt nose, and its diameter is fixed at 2 mm. A flat aerodisk is installed in front of the aerospike. In order to evaluate drag reduction effects during the dynamic process, the aerospike length and aerodisk diameter are variable. The cases of the oscillation period, aerospike length, and aerodisk diameter are shown in Table 1.

Before the dynamic simulation, we prepare a steady convergent flow field without angle of attack and use it as the initial field for unsteady computation. The aircrafts undergo forced-pitching oscillation around the mass center of the blunt head, which is located on the axis and 0.1786 D from the apex. The kinematic law can be written as

$$\theta = \theta_0 \sin (kt), \qquad (1)$$

where $\theta_0$ is the amplitude and $k$ represents the reduced frequency.

The parameters of incoming flow are consistent with the experimental conditions (Mach number of 5.75 and static temperature of 140 K). The wall is isothermal, and its temperature is 300 K. Other conditions of incoming flow are shown in Table 2.

TABLE 3: First-layer grid height of the aircraft wall surface.

| Characteristic | First-layer grid height/mm | Re$_{grid}$ |
|---|---|---|
| Coarse | 0.03 | 46 |
| Moderate | 0.003 | 4.6 |
| Refined | 0.0003 | 0.46 |

*2.2. Numerical Method for Unsteady Flow Simulation.* Forced-pitching oscillation of aircraft involves the motion of grid boundary. To accurately describe the flow of the moving boundary, we establish the coordinate system on the basis of the arbitrary-Lagrangian-Eulerian (ALE) method. The integral governing equations are expressed in the ALE formulation:

$$\frac{\partial}{\partial t} \int_V U dV + \oint_S \left(F - U v_g \cdot n\right) dS = \oint_S F^v dS, \qquad (2)$$

where $U$ denotes the conservation variables vector and $F$ and $F^v$ represent the inviscid and viscid flux vectors, respectively. $v_g$ stands for the velocity of the moving face. $dV$ symbolizes the control volume and its surface area notes $dS$, the unit normal direction of which is $n$.

For the purposes of this study, the forced-pitching oscillation of the aircraft is a hydrodynamics/kinematics coupling problem. In order to ensure stability, we adopt the strong coupling method (see Figure 2). In addition, to assure the time accuracy of the numerical simulation, we introduce the dual-time stepping strategy and LU-SGS implicit time-marching method:

$$\frac{\partial}{\partial \tau} \int_V U dV + \frac{\partial}{\partial t} \int_V U dV + \oint_S \left(F - U v_g \cdot n\right) dS = \oint_S F^v dS, \qquad (3)$$
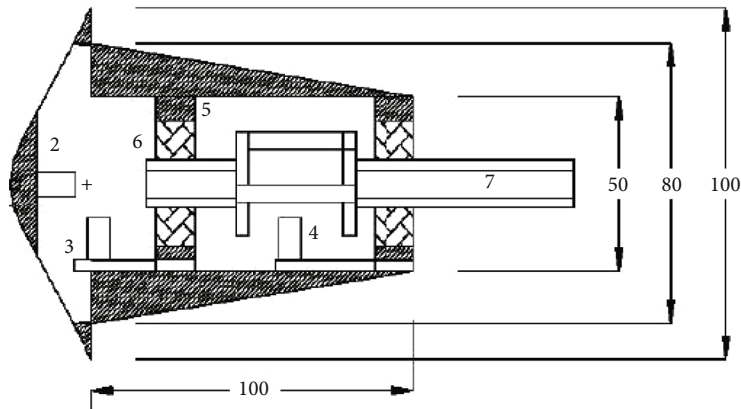
FIGURE 4: Experimental model.

TABLE 4: Comparison of drag coefficients between numerical simulation and experiment.

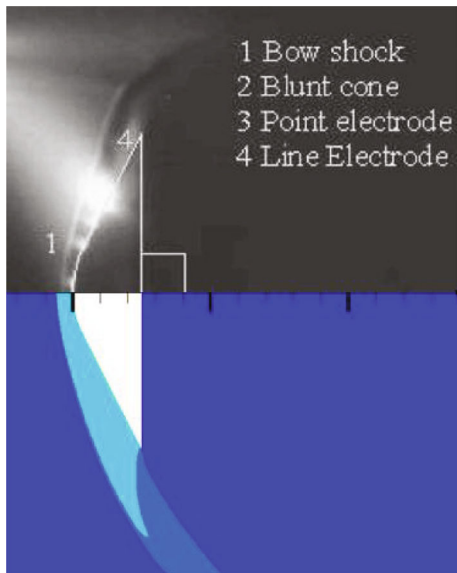| Case number | First-layer grid height/ mm | Turbulent model | Far-field mesh | Surface mesh | Numerical drag coefficient | Deviation with experiment |
|---|---|---|---|---|---|---|
| Exp. | | | | | 1.462 | |
| 1 | 0.03 | SST | Moderate | Moderate | 1.5266 | 4.42% |
| 2 | 0.03 | SA | Moderate | Moderate | 1.5264 | 4.40% |
| 3 | 0.003 | SST | Moderate | Moderate | 1.5163 | 3.71% |
| 4 | 0.003 | SA | Moderate | Moderate | 1.5159 | 3.69% |
| 5 | 0.0003 | SST | Moderate | Moderate | 1.5030 | 2.80% |
| 6 | 0.0003 | SA | Moderate | Moderate | 1.5012 | 2.68% |
| 7 | 0.003 | SA | Coarse | Moderate | 1.5204 | 3.99% |
| 8 | 0.003 | SA | Refined | Moderate | 1.5154 | 3.65% |
| 9 | 0.003 | SA | Moderate | Coarse | 1.5279 | 4.51% |
| 10 | 0.003 | SA | Moderate | Refined | 1.5144 | 3.58% |



FIGURE 5: Comparison between the numerical contour and experimental schlieren picture.



- · - Without spike-T62.5
- - - Without spike-T125
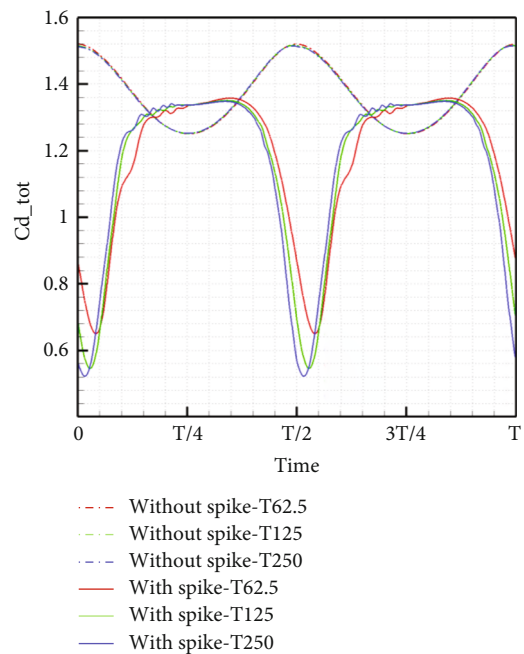- · - Without spike-T250
— With spike-T62.5
— With spike-T125
— With spike-T250

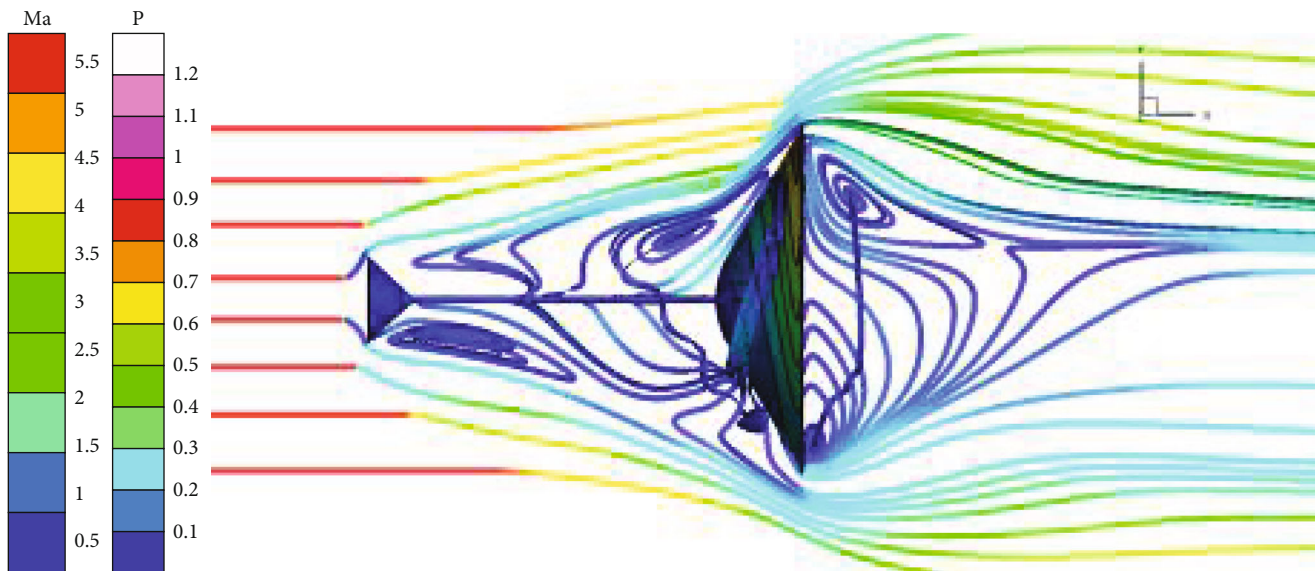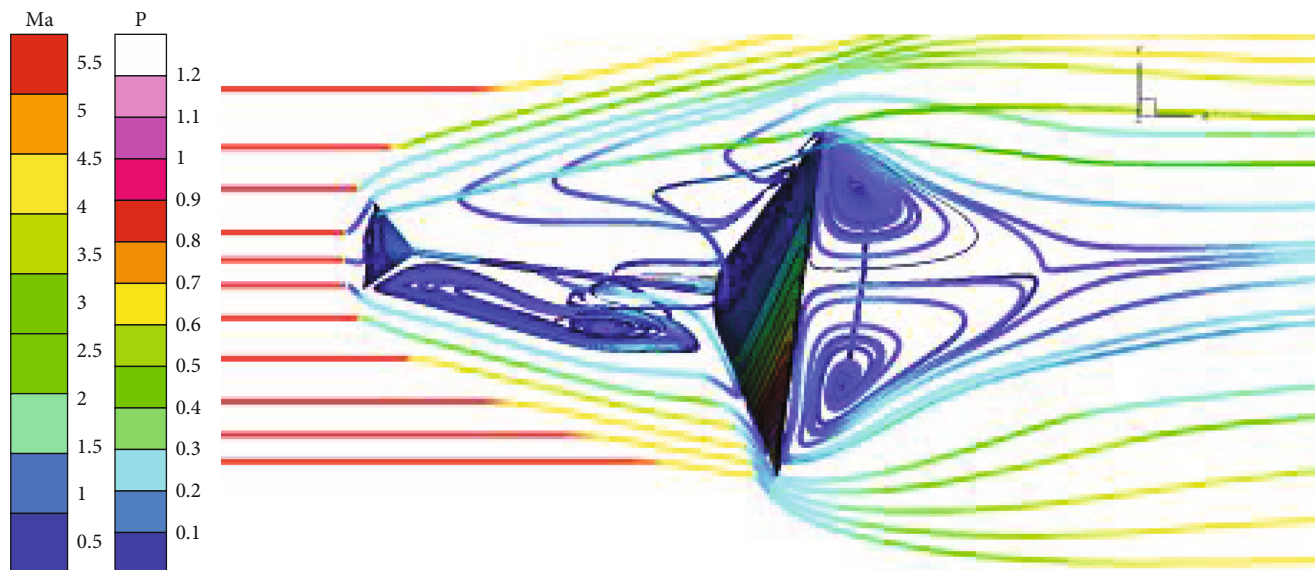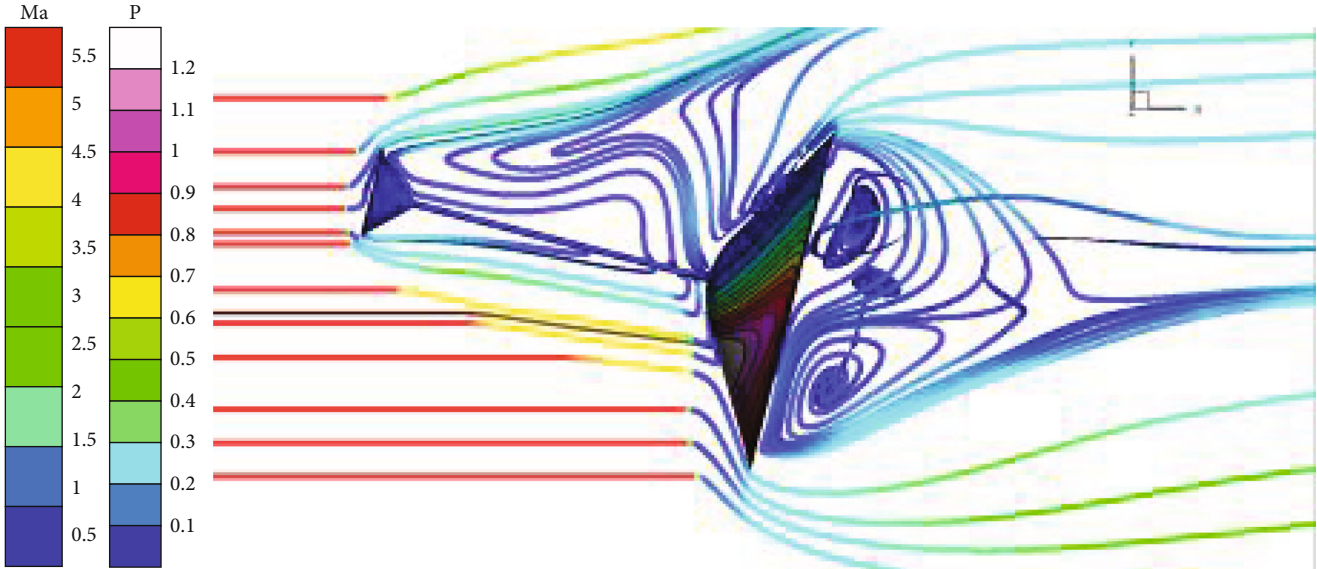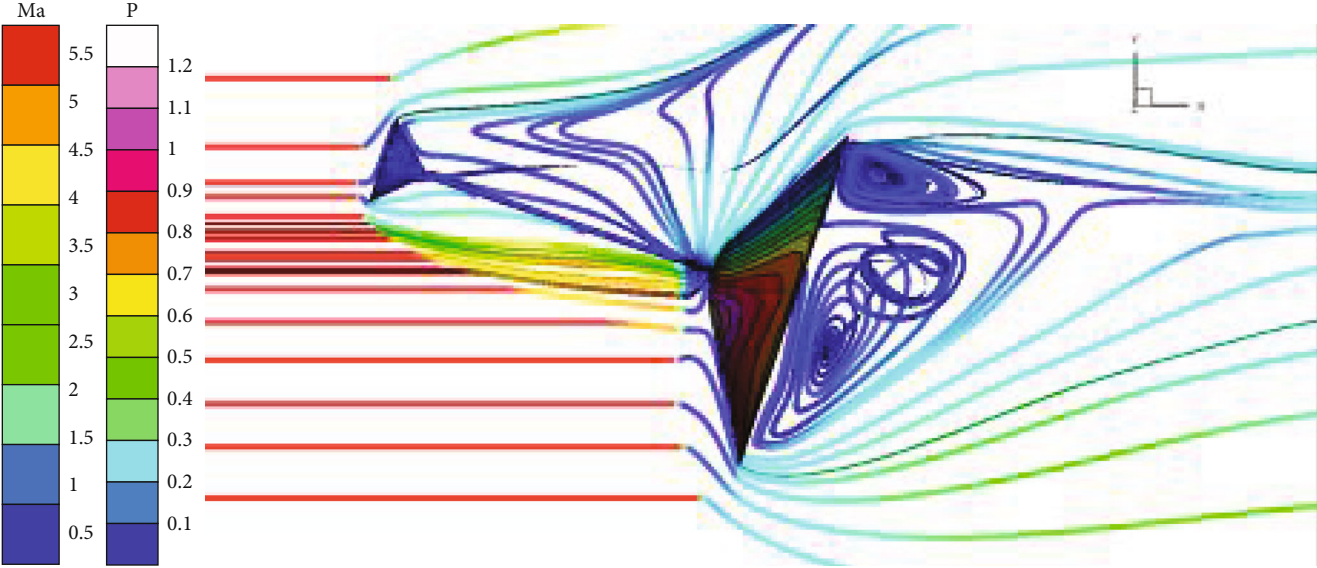FIGURE 6: Development of drag coefficient.
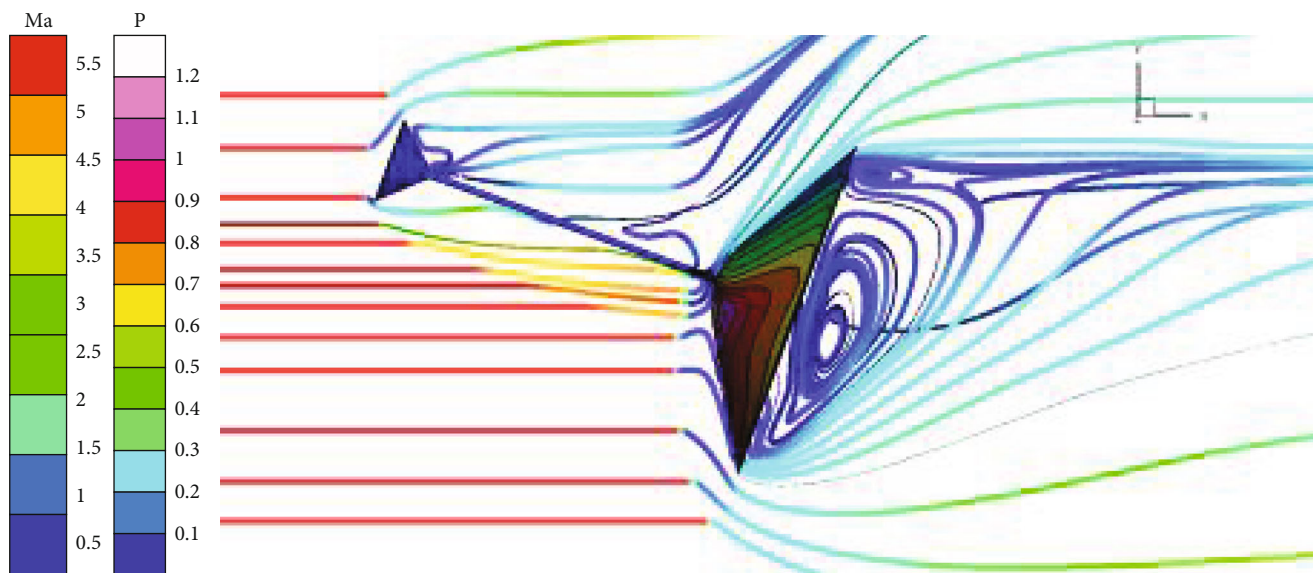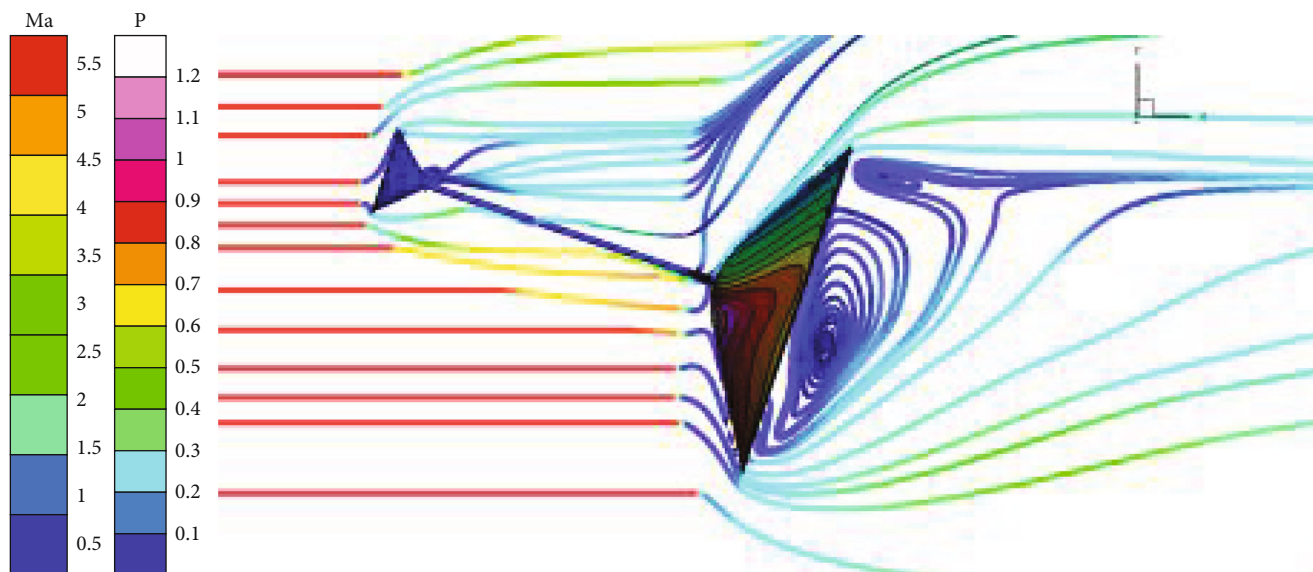
(a)



(b)

FIGURE 7: Continued.

(c)
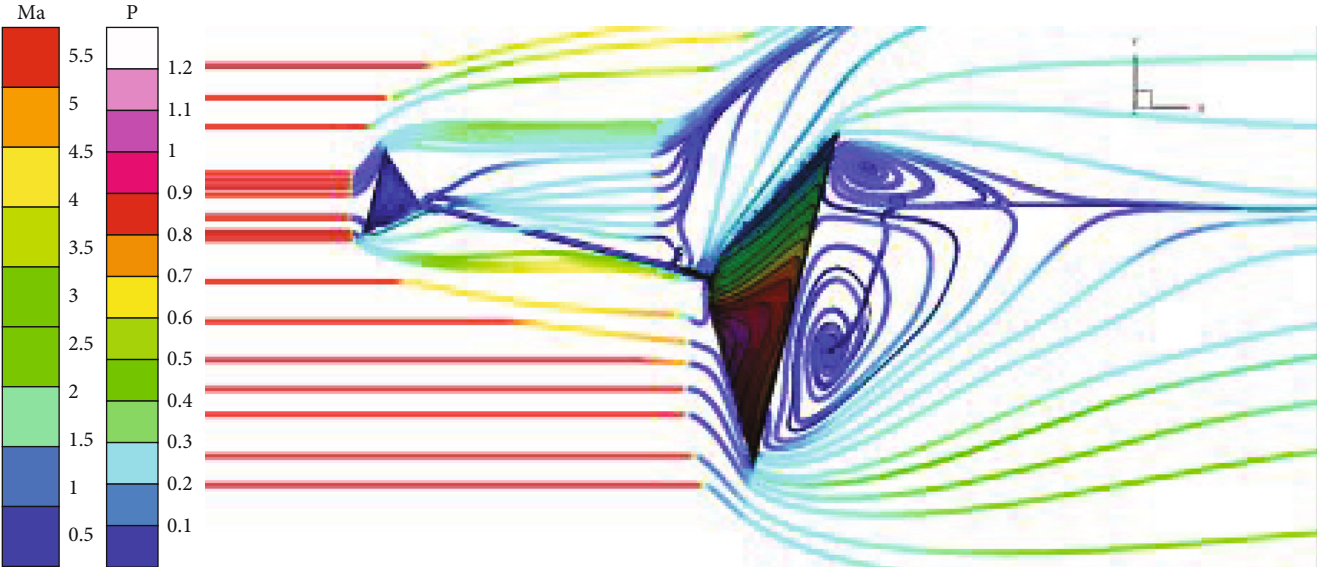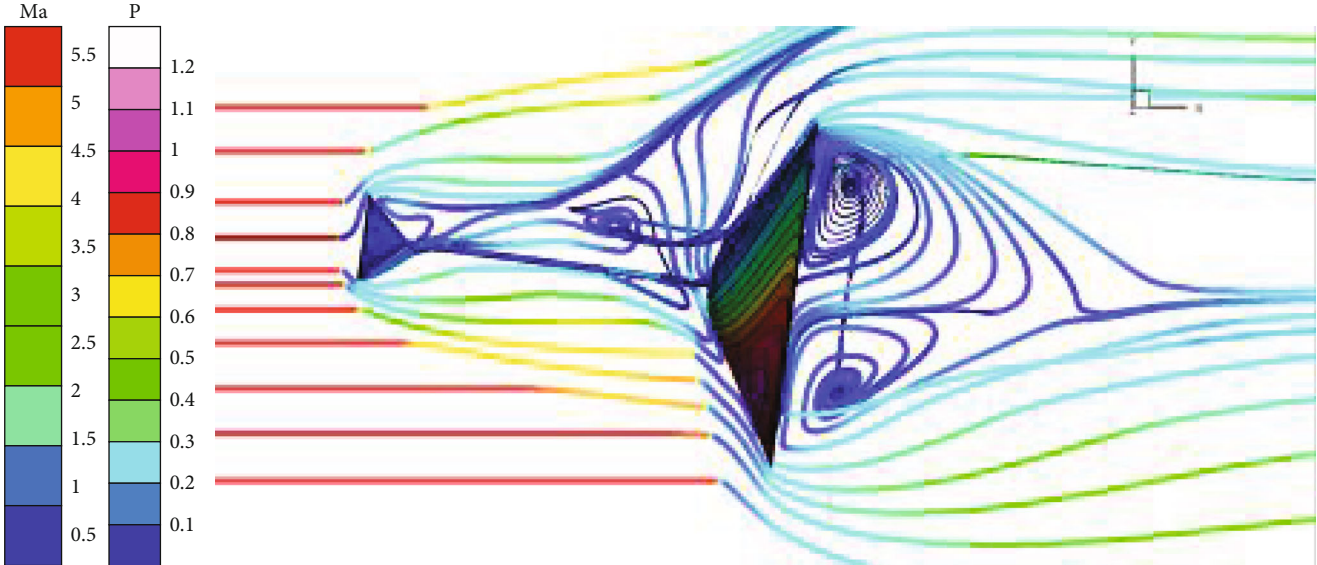


(d)

Figure 7: Continued.

(e)



(f)

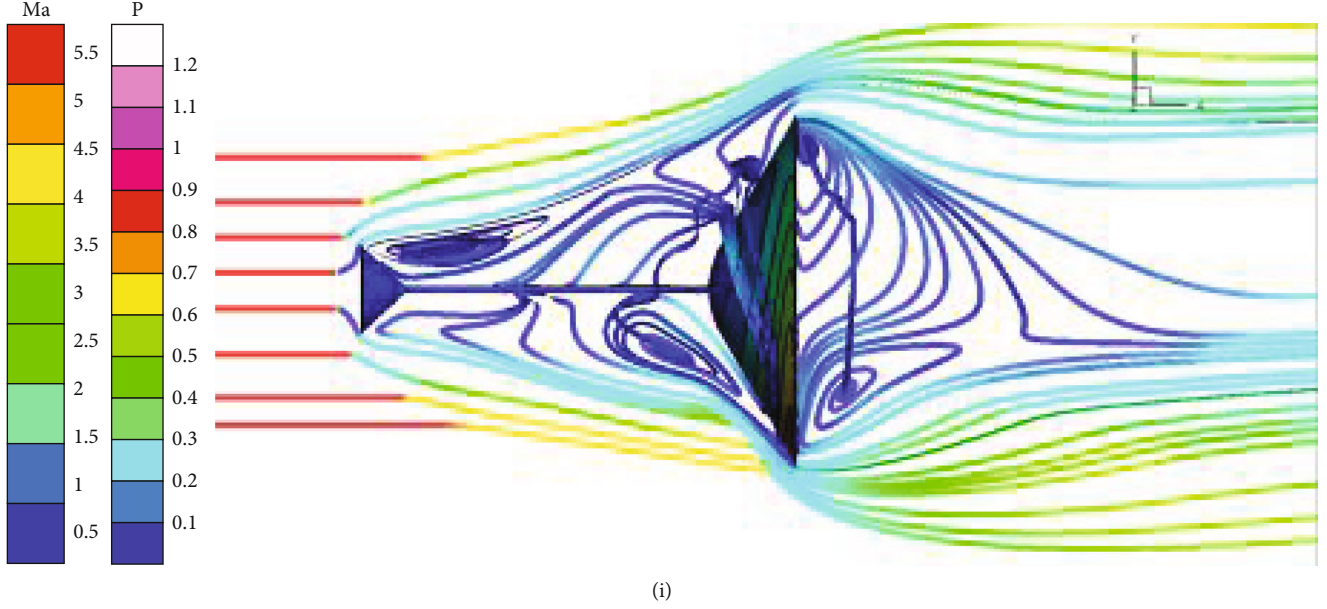FIGURE 7: Continued.

(g)



(h)

FIGURE 7: Continued.

(i)

FIGURE 7: Instantaneous streamline (stained by Mach number) and wall pressure contour of forced-pitching oscillation. (a) Pitch angle 0°; phase angle 0°. (b) Pitch angle 7.7°; phase angle 22.5°. (c) Pitch angle 14.1°; phase angle 45°. (d) Pitch angle 18.5°; phase angle 67.5°. (e) Pitch angle 20°; phase angle 90°. (f) Pitch angle 18.5°; phase angle 112.5°. (g) Pitch angle 14.1°; phase angle 135°. (h) Pitch angle 7.7°; phase angle 157.5°. (i) Pitch angle 0°; phase angle 180°.

where $\tau$ represents the pseudotime, and the subiteration number is set to 80 in the calculation.

The solution of the governing equation is based on the finite volume method. After integrating Equation (3) on the control volume, we can get

$$\frac{\partial}{\partial \tau}(\boldsymbol{U}V) + \frac{\partial}{\partial t}(\boldsymbol{U}V) + \sum_i \left(\boldsymbol{F} - \boldsymbol{U}\boldsymbol{v}_g \cdot \boldsymbol{n}\right)dS_i = \sum_i \boldsymbol{F}^v dS_i. \quad (4)$$

Taking the first-order backward Euler scheme as an example, Equation (4) transforms into the following equation after discretization of the temporal terms:

$$\frac{\boldsymbol{U}^{m+1}V^{n+1} - \boldsymbol{U}^m V^{n+1}}{\Delta \tau} + \frac{\boldsymbol{U}^{m+1}V^{n+1} - \boldsymbol{U}^n V^n}{\Delta t} + \text{RHS}^{m+1} = 0, \quad (5)$$

where $m$ represents the subiteration and $n$ is the physical time iteration. $RHS$ denotes the sum of the inviscid and viscid flux vectors, which can be expressed as

$$\text{RHS} = \sum_i \left(\boldsymbol{F} - \boldsymbol{U}\boldsymbol{v}_g \cdot \boldsymbol{n}\right)dS_i - \sum_i \boldsymbol{F}^v dS_i. \quad (6)$$

We split the difference for the inviscid and viscid flux vectors based on Roe's scheme and used the one-equation SA model for the turbulent solution. The surface of the aircraft is a nonslip wall, and the far-field boundary is handled with the nonreflection approach. These methods have been integrated into our unsteady RANS solver. For more details, please refer to Zhang and Wang [24] and Chang et al. [25].

2.3. Grid Setup. To deal with the moving boundary problem, we adopt the dynamic overlapping grid technique for our calculations. The basic idea of this method is to begin by generating mesh for different objects separately. Obviously, there will be overlapped regions between grid blocks. Therefore, it is necessary to preprocess the grid before the calculation. For example, the transfer relationship between flow variables is established on the boundary of overlapping domains. The boundary information is updated by data interpolation and exchanges at the beginning of calculation. Then, the solution of the whole flow field can be obtained after time advancing.

As shown in Figure 3(a), the grid setup uses hybrid structure-unstructured grids. To accurately ensure the first cell distance order, the body-fitted mesh near the wall surface adopts hexahedral grids. The outer mesh is the unstructured one, which could be generated automatically with Pointwise software. Furthermore, to realize parallel computation and improve computing efficiency, the grid is partitioned before simulation (as shown in Figure 3).

In addition, we use three sets of grids to verify grid independence and compare the simulation results with the experimental data. The first cell distance and grid Reynolds number of the coarse, moderate, and refined grids are listed in Table 3. The wall grid Reynolds number is defined in Equation (7).

$$\text{Re}_{\text{grid}} = \frac{\rho_\infty v_\infty \Delta x}{\mu_\infty}, \quad (7)$$

where $\rho_\infty$, $v_\infty$, and $\mu_\infty$ represent the density, velocity, and
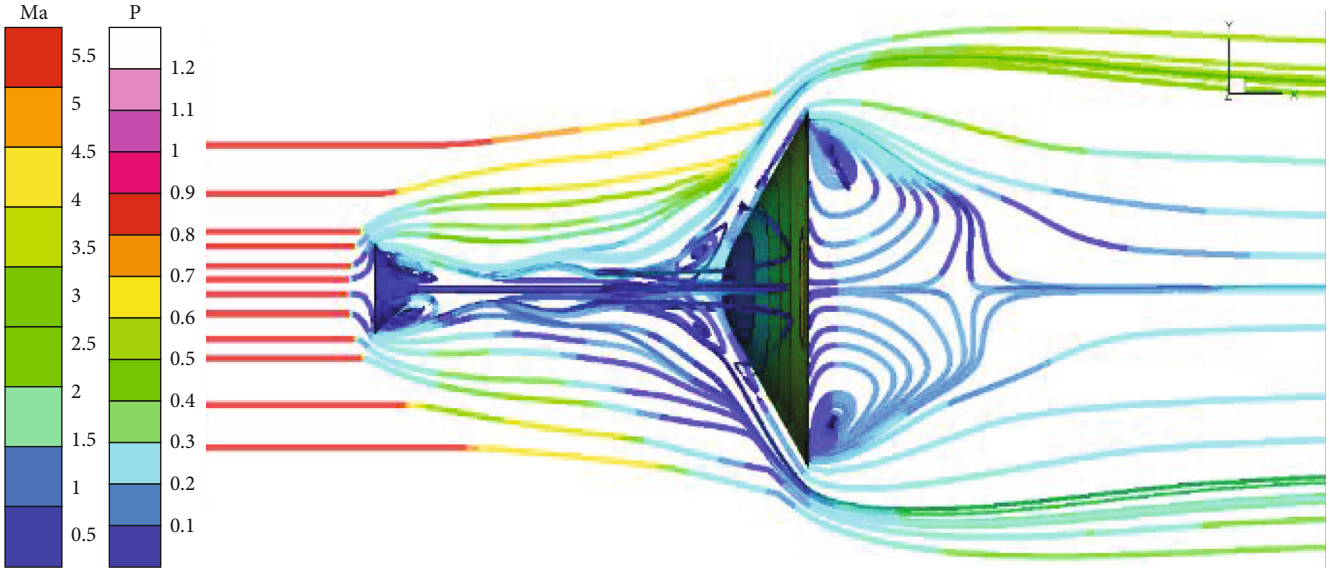
FIGURE 8: Time-averaged streamline (pitch angle 0°; phase angle 0°).

viscosity coefficients of the incoming flow, respectively. $\Delta x$ is the first cell distance near the wall surface.

2.4. Solver Validation. We simulate the blunt body without the spike used by Menezes et al. [8] in their experiment in order to validate our numerical method. The experimental geometric model is shown in Figure 4. We adopt one-equation SA and two-equation SST turbulent models to simulate the three sets of grids mentioned above. After simulation, we calculate the drag coefficients and compared them with the experimental values. In addition, we compared the density contour from simulation to the schlieren picture from the experiment.

The comparison between the drag coefficients obtained from simulation and experiment is shown in Table 4, and the results show that there is little difference between the experimental and computed data. The one-equation SA turbulent model performs a little better than the SST model. Besides, various researches show that the one-equation Spalart-Allmaras turbulence model presents valid data in simulating the high-speed turbulent flows [18, 26]. Paciorri et al. [27] focused on the validity of this turbulence model in hypersonic flows and declared that this model had reasonable accuracy in prediction of surface pressure.

The drag coefficient difference between three sets of grids is negligible as the evidence of grid convergency. By decreasing first cell distance, the $Cd$ obtained by simulation is closer to the experimental result, despite the fact of higher computational expense. In addition, when refining the grid in surface or far-field, the numerical drag coefficient also gets closer to that from experiment. After balancing the amount and accuracy of calculation, the moderate mesh of surface, far-field, and the first-layer is the most suitable for subsequent simulation.

Therefore, the moderate mesh is adopted in this paper, along with the one-equation SA turbulent model.

TABLE 5: Average drag reduction conditions of aircraft with different $L/D$.

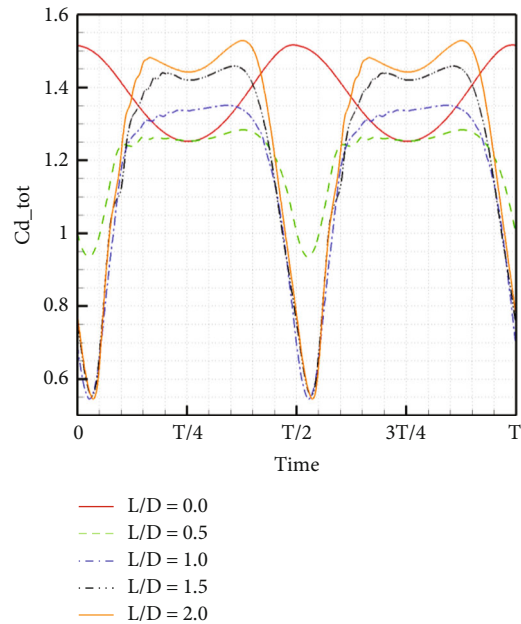| $L/D$ | $d/D$ | Average drag coefficient ($Cd$) | Average drag reduction rate/% |
|---|---|---|---|
| 0.0 | 0.0 | 1.3761 | 0.00 |
| 0.5 | 0.25 | 1.2030 | 12.58 |
| 1.0 | 0.25 | 1.1623 | 15.54 |
| 1.5 | 0.25 | 1.2280 | 10.76 |
| 2.0 | 0.25 | 1.2727 | 7.51 |



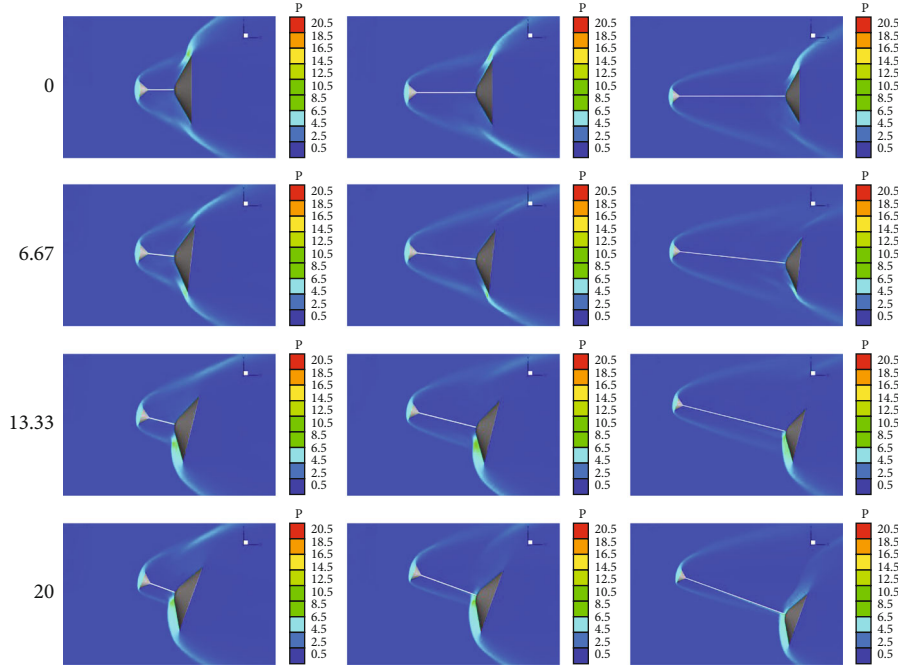FIGURE 9: Development of the drag coefficient with different $L/D$.

FIGURE 10: Development of the flow-field density contour with different $L/D$.

Figure 5 shows the comparison between the schlieren picture and density contour obtained under the condition of $\Delta x = 0.003$ mm with the SA model. It can be observed that the detached shock position derived from the steady-state computation matches fairly well with the reported experimental result. Therefore, our grid and simulation tool are validated, and the following calculation results are reliable.

## 3. Results and Discussion

*3.1. Effect of Oscillation Period.* As shown in Figure 6, to compare the effect of pitching oscillation period on aircraft resistance characteristics, the dimensional periods are set to 62.5 s, 125 s, and 250 s. It is found that the drag coefficient of an aircraft without an aerospike is scarcely affected by the oscillation period. After mounting an aerospike with an aerodisk, the numerical values for different periods show little difference, either. However, a distinct phase delay exists in the variation curves of $Cd$, especially when the pitch angle was is around 0°.

In order to explain this difference, we first analyse the flow field evolution around the aircraft. Figure 7 depicts the streamlines in the symmetry plane. Nine instantaneous flow fields are listed, all of which are from the first half period of the fourth oscillation cycle (when the resonance flow is stable). The relation between phase angle and pitch angle is described by Equation (1).

Figure 7(a) depicts the streamlines at 0° pitching angle and 0° phase angle, and the flow looks asymmetric. However, as Figure 8 shows, the time-averaged streamlines and contour get symmetric. It could be deduced that the flow during the pitching oscillation is kept in a highly unsteady state, causing the asymmetric behaviour. And the phase delay phe-
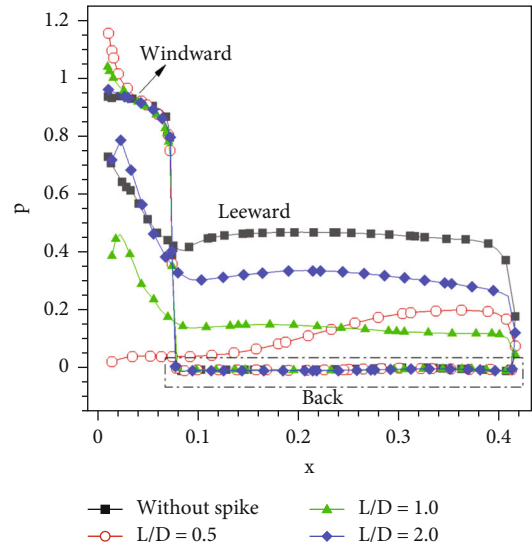


FIGURE 11: Wall pressure distribution of a blunt body at a pitch angle of 20°.

nomenon might be one of the prime reasons. The subsequent figures show progressively increasing phase angle intervals (in increments of 22.5°). The afterbody flow is asymmetrical at a zero-degree pitch angle. At that point, the lower vortex is dominant, which leads to the impingement by the inverse flow on the upper part of the blunt body base. The recirculation region extended backward to 0.636 D. When the pitch angle increases to 7.7°, the backflow impinges near the center of the rear body. The above phenomena indicate that during unsteady oscillation, there is a large phase delay in the flow around the afterbody. As shown
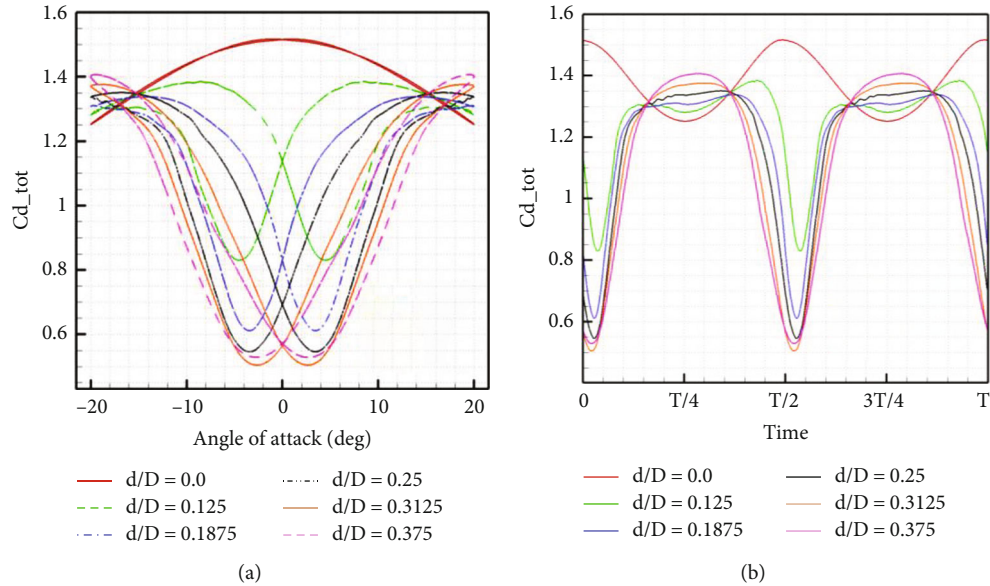
FIGURE 12: Development of the drag coefficient with different $d/D$. (a) Drag coefficients varying with attack angle. (b) Drag coefficients varying with time.

in Figure 6, decreasing the oscillation period will strengthen the phase delay in the flow field.

Additionally, the recirculation region in front of the aircraft has an important influence on the drag characteristics. Figure 7 illustrates that the drag coefficient will decrease when the recirculation region develops fully (especially near a pitch angle of 0°), and a large $Cd$ value is corresponded to the moment of windward recirculation zone disappearance. The shape of the recirculation zone in front of the aircraft is regular in a steady state. Generally speaking, the larger the recirculation zone, the better the drag reduction effect. When undergoing pitching oscillation, the recirculation region distribution on both sides of the aerospike is obviously less regular than that in the steady state. Under higher pitch angle, the conical shock wave in the leeward region expands outward gradually, destructing the recirculation zone. In the meantime, the windward conical shock wave moves closer to the aerospike surface. Due to direct impingement of the incoming flow, the area of the recirculation zone begins to decrease, almost becoming zero near a pitch angle of 14.1°.

It can be concluded that the value of $Cd$ is decided by the area of the recirculation zone, while the afterbody flow causes the phase delay phenomenon.

*3.2. Effect of Aerospike Length.* Table 5 shows that the four aerospike lengths (mounted with an aerodisk) all could achieve the goal of drag reduction. When $L/D = 1.0$ ($L/D$ represents the ratio of aerospike length and blunt diameter), the minimum average drag coefficient is obtained; the least value is 15.54%. After $L/D > 1.0$, the average reduction rate will decrease with the increase of $L/D$.

As shown in Figure 9, the drag reduction effect of aerospikes with various lengths is different with various pitch angles during the pitching oscillation. When the pitch angle is small ($|\theta| < 9°$), the 0.5 D aerospike performs less effectively in drag

reduction. The other three aerospike configurations show little difference. With a high pitch angle ($|\theta| > 13°$), the drag coefficient of aircraft is proportional to $L/D$; when the pitch angle goes up to around 20°, only the $L/D = 0.5$ configuration can attain the object of drag reduction.

Figure 10 depicts the flow field density contour when the ratios of aerospike length and blunt diameter are 0.5, 1.0, and 2.0. When the pitch angle is small, for example, 0° or 6.67°, the recirculation zone of $L/D = 0.5$ configuration is too small to surround the whole surface of the blunt forebody. When the value of $L/D$ increases to 1.0 or 2.0, the front of the blunt aircraft is completely covered by the conical shock wave. The recirculation inside the conical shock wave significantly reduces the pressure on the front wall. Therefore, when the angle of pitching oscillation is less than 9°, aircrafts with aerospikes perform ideally with configurations other than $L/D = 0.5$.

When the angle of attack goes up to 20°, the windward side of the blunt body is exposed out of the conical shock wave. As a result, the windward wall surface pressure increases significantly. The distribution of wall surface pressure is shown in Figure 11. Due to the protection from the bow shock wave, the head wall pressure of the aircraft without an aerospike is comparatively small. In addition, there is a recirculation region on the leeward side, which leads to a lower wall pressure level. Under the function together with the windward and leeward, the pressure drag while $L/D = 0.5$ is not higher than that of the blunt aircraft without an aerospike. With the increase of $L/D$, the reattachment shock wave approaches the wall gradually. As shown in Figure 11, the strength of the reattached shock wave goes up. The flow is subjected to a stronger compression effect, which increases the pressure of the front wall, and the pressure difference between the front and back walls rises. Consequently, the configuration of $L/D = 1.0$ and $L/D = 2.0$ is not effective for drag reduction.
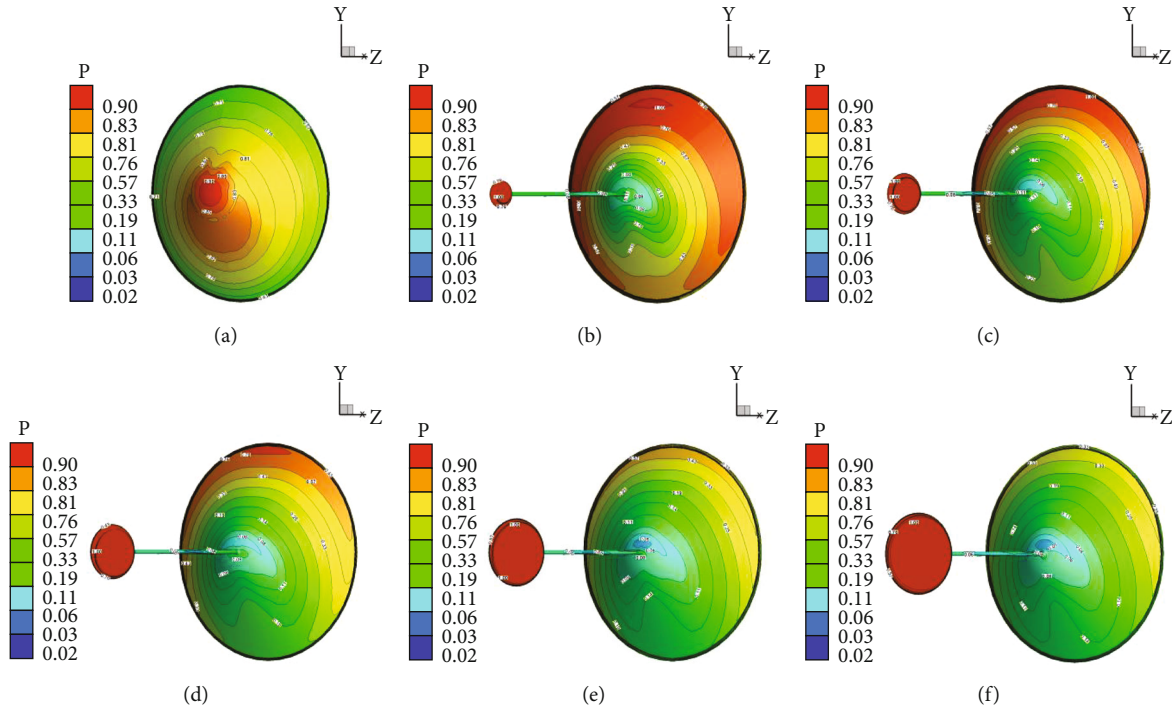
FIGURE 13: Wall pressure contour at a pitch angle of 0°. (a) $d/D = 0.0$. (b) $d/D = 0.125$. (c) $d/D = 0.1875$. (d) $d/D = 0.25$. (e) $d/D = 0.3125$. (f) $d/D = 0.375$.
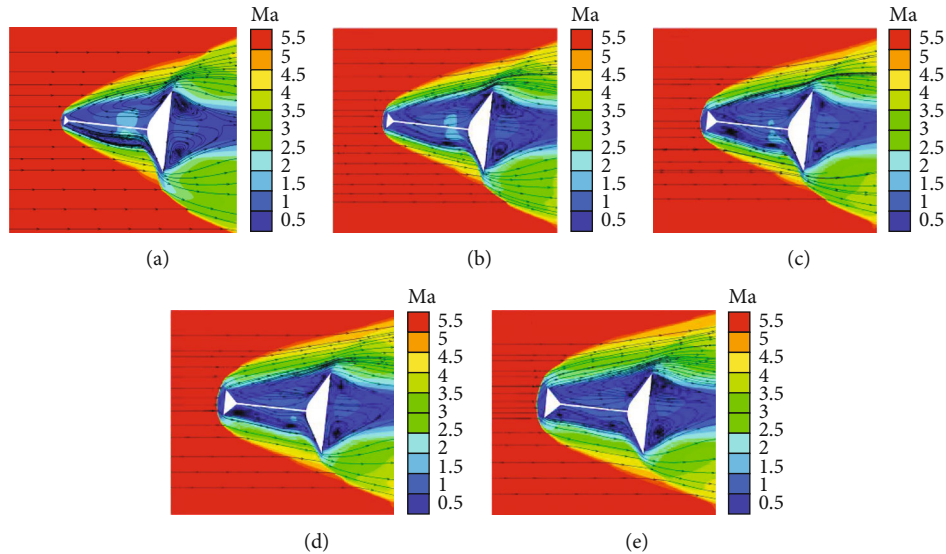


FIGURE 14: Mach number contours and streamline diagrams of different $d/D$ at a pitch angle of 6.67°. (a) $d/D = 0.125$. (b) $d/D = 0.1875$. (c) $d/D = 0.25$. (d) $d/D = 0.3125$. (e) $d/D = 0.375$.

### 3.3. Effect of Aerodisk Diameter.

The literature indicates that the size of the aerodisk also has an important effect on drag reduction. In this section, we explore how aerodisk diameter influences pressure drag during the dynamic process. Figure 12 illustrates the drag coefficient with a configuration of $d/D = 0.125, 0.1875, 0.25, 0.3125$, and $0.375$ ($d/D$ represents the ratio of aerodisk diameter and blunt diameter). During pitching oscillation, the dynamic characteristic varies with the change of angle of attack.

Near a pitch angle of 0° ($|\theta| < 5°$), the drag coefficient decreases with the increase of $d/D$ until $d/D > 0.3125$. It also fluctuates within a narrow range after $d/D = 0.3125$, so that drag reduction could be achieved when the aerodisk diameter is 0.3125 D. In the medium pitch angle range, the pressure drag will be reduced further by a bigger aerospike. The drag reduction rate maintains an upward tendency as the pitch angle goes down. With a pitching oscillation angle around 20° ($|\theta| > 17°$), all the aerospikes evaluated will bring about extradrag compared to the blunt body. The
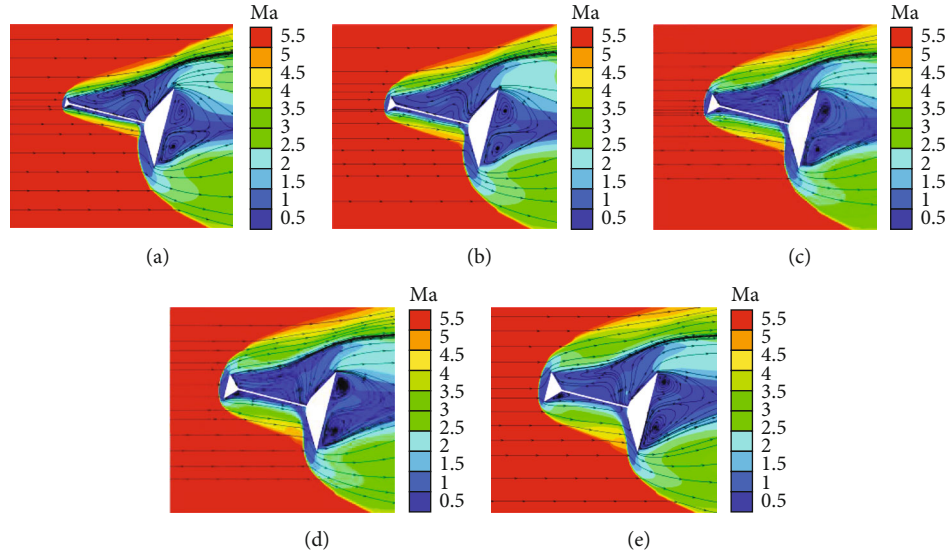
FIGURE 15: Mach number contours and streamline diagrams of different $d/D$ at a pitch angle of 13.33°. (a) $d/D = 0.125$. (b) $d/D = 0.1875$. (c) $d/D = 0.25$. (d) $d/D = 0.3125$. (e) $d/D = 0.375$.

greater the value of $d/D$, the more the increase of drag coefficient.

The aerospikes will expand the circulation ahead of the blunt body, which significantly reduces the pressure near the stagnation point of the blunt nose. Figure 13 shows the wall surface pressure contours at zero angle of attack. The conical shock wave directly impinges on the blunt body shoulder, causing the pressure increment. When $d/D \leq 0.3125$, the conical shock wave is pushed away from the surface by the aerodisk, and as the aerodisk diameter increases, the cone angle of the shock wave goes up. The forebody surface pressure will descend as well. As a consequence, when nearing zero pitch angle, the drag coefficient decreases with the increase of $d/D$. When the aerodisk diameter goes up to 0.3125 D and 0.375 D, the conical shock wave is far away from the wall. The increase in aerodisk diameter has little effect on the recirculation region. Therefore, the drag coefficient of $d/D = 0.3125$ is similar to that of $d/D = 0.375$.

Near the midrange of pitch angle, the aircraft with a large-diameter aerodisk could attain a high drag reduction rate. The Mach contours at pitch angles of 6.67° and 13.33° are shown in Figures 14 and 15. With the enhancement of pitch angle, the shear layer under the aerospike starts to approach the spike surface. Also, during high-angle pitching oscillation, the area of the recirculation region declines dramatically, leading to higher drag coefficients. Nevertheless, a large-diameter aerospike will relieve this tendency. Accordingly, as the value of $d/D$ increases, the drag reduction rate will rise.

When the pitch angle rises to 20°, there is no recirculation zone beneath the aerospike. The windward side of the blunt body is impinged on directly by the incoming flow. As shown in Figure 16, the wall pressure is high on the windward side. The difference in pressure of the windward region with different $d/D$ configurations is small. In addition, with higher $d/D$ values, the leeward recirculation area will become larger and the pressure near the blunt wall will be
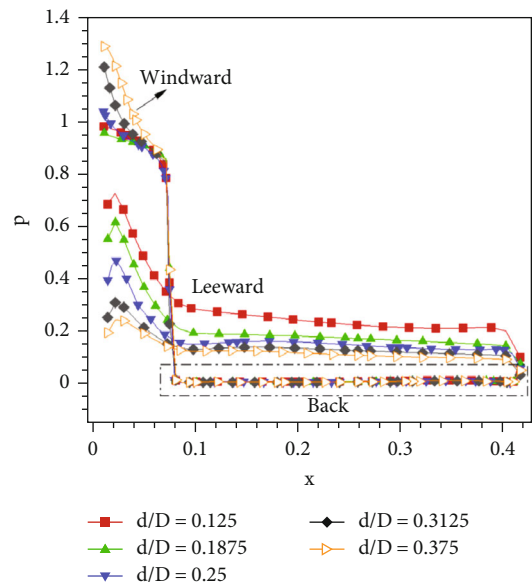


FIGURE 16: Wall pressure distribution of a blunt body at a pitch angle of 20°.

reduced. The pressure at the back of the blunt body is low and not affected by the aerodisk diameter. Therefore, the larger the aerodisk diameter, the greater the pressure drag on the aircraft.

## 4. Conclusions

A detailed computational study on the dynamic performance of blunt bodies with aerospikes and aerodisks has been carried out. We choose pitching oscillation simulation, a common model in dynamics researches, and primarily consider how oscillation period, amplitude, aerospike length, and aerodisk diameter affect the drag characteristics of

aircraft. We also comprehensively analyze the impact of these parameters on the flow field around the blunt body.

The major conclusions from the present study are as follows:

(1) During unsteady pitching oscillation, there is a phase delay phenomenon in the flow field behind the blunt body. This phenomenon becomes more obvious when the oscillation period is decreased. In addition, the value of the drag coefficient is primarily influenced by the area of the recirculation zone on either side of the aerospike. The optimum drag reduction effect is obtained with a fully developed recirculation region. The recirculation zone on the windward side disappears when the pitch angle is large, leading to a higher drag coefficient

(2) The impact of aerospike length on drag characteristics is linked to the pitch angle. This finding contrasts with the law previously discovered under the steady state. At a pitch angle of 9°, the drag reduction effect is worse when the aerospike length is 0.5 D. There is little difference between the configurations of $L/D = 1.0$, 1.5, and 2.0, all of which can perform ideally on drag reduction. When $|\theta| > 13°$, the drag reduction rate will decrease with the enhancement of $L/D$. Only the configuration $L/D = 0.5$ can attain the objective of drag reduction when the pitch angle is near 20°

(3) When the angle of pitching oscillation declines to approximately 0°, the drag reduction rate displays an upward tendency with the increase of aerodisk diameter until $d/D = 0.3125$ and remains almost the same after that. At a midrange pitch angle, the larger the aerodisk size, the smaller the value of the drag coefficient. However, when the pitch angle rises above 17°, the aerospike cannot reduce drag. Finally, the drag of aircraft will rise with increased $d/D$

## Data Availability

The data used to support the findings of this study are available from the corresponding author upon request.

## Conflicts of Interest

The authors declare that there is no conflict of interest regarding the publication of this paper.

## Acknowledgments

## References

[1] D. M. Bushnell, "Shock wave drag reduction," *Annual Review of Fluid Mechanics*, vol. 36, no. 1, pp. 81–96, 2004.

[2] W. Huang, "A survey of drag and heat reduction in supersonic flows by a counterflowing jet and its combinations," *Journal of Zhejiang University SCIENCE A*, vol. 16, no. 7, pp. 551–561, 2015.

[3] H. X. Zhang and J. Huang, "Numerical simulation of hypersonic flow over axisymmetric spiked body," *Acta Aeronautica et Astronautica Sinica*, vol. 15, no. 5, pp. 519–525, 1994, (In Chinese).

[4] S. R. Alexander, *Results of Tests of Determine the Effect of a Conical Windshield on the Drag of a Bluff Body at Supersonic Speeds*, National Aeronautics and Space Administration Hampton Va Langley Research Center, 1947.

[5] R. O. Piland and L. W. Putland, *Zero-Lift Drag of Several Conical and Blunt Nose Shapes Obtained in Free Flight at Mach Numbers of 0.7 to 1.3*, Technical report archive & image library, 1956.

[6] W. A. Mair, "LXVIII. Experiments on separation of boundary layers on probes in front of blunt-nosed bodies in a supersonic air stream," *The London, Edinburgh, and Dublin Philosophical Magazine and Journal of Science*, vol. 43, no. 342, pp. 695–716, 1952.

[7] C. J. Wood, "Hypersonic flow over spiked cones," *Journal of Fluid Mechanics*, vol. 12, no. 4, pp. 614–624, 1962.

[8] V. Menezes, S. Saravanan, G. Jagadeesh, and K. P. J. Reddy, "Experimental investigations of hypersonic flow over highly blunted cones with aerospikes," *AIAA Journal*, vol. 41, no. 10, pp. 1955–1966, 2003.

[9] S. M. Bogdonoff and I. E. Vas, "Preliminary investigations of spiked bodies at hypersonic speeds," *Journal of the Aerospace Sciences*, vol. 26, no. 2, pp. 65–74, 1959.

[10] D. Crawford, *Investigation of the Flow over a Spiked-Nose Hemisphere-Cylinder at a Mach Number of 6.8*, National Aeronautics and Space Administration Washington, 1960.

[11] W. E. Thurman, "A flow-separation spike for hypersonic control of a hemisphere-cylinder," *AIAA Journal*, vol. 2, no. 1, pp. 159–161, 1971.

[12] P. Gnemmi, J. Srulijes, K. Roussel, and K. Runne, "Flowfield around spike-tipped bodies for high attack angles at Mach 4.5," *Journal of Spacecraft and Rockets*, vol. 40, no. 5, pp. 622–631, 2003.

[13] R. Kalimuthu, R. C. Mehta, and E. Rathakrishnan, "Experimental investigation on spiked body in hypersonic flow," *Aeronautical Journal*, vol. 112, no. 1136, pp. 593–598, 2008.

[14] W. Jiang, Y. J. Yang, and H. W. Chen, "Investigations on aerodynamics of the spike-tipped hypersonic vehicles," *Journal of Experiments in Fluid Mechanics*, vol. 25, no. 6, pp. 30–34+55, 2011, (In Chinese).

[15] M. Yamauchi, K. Fujii, and F. Higashino, "Numerical investigation of supersonic flows around a spiked blunt body," *Journal of Spacecraft and Rockets*, vol. 32, no. 1, pp. 32–42, 1995.

[16] M. B. Gerdroodbary and S. M. Hosseinalipour, "Numerical simulation of hypersonic flow over highly blunted cones with spike," *Acta Astronautica*, vol. 67, no. 1-2, pp. 180–193, 2010.

[17] J. J. Sebastian, A. Suryan, and H. D. Kim, "Numerical analysis of hypersonic flow past blunt bodies with aerospikes," *Journal of Spacecraft & Rockets*, vol. 53, no. 4, pp. 669–677, 2016.

[18] M. Kharati-Koopaee and H. Gazor, "Assessment of the aerodisk size on drag reduction and thermal protection of high-bluntness vehicles at hypersonic speeds," *Journal of Aerospace Engineering*, vol. 30, no. 4, 2017.

[19] A. Narayan, S. Narayanan, R. Kumar, C. S. Kumar, and G. Jagadeesh, "Hypersonic flow past a spherically blunted nose cone: a computational study," *Progress in Computational Fluid Dynamics*, vol. 20, no. 2, pp. 105–123, 2020.

[20] H. L. Zhao, K. Peng, Z. P. Wu, W. H. Zhang, J. W. Yang, and J. B. Sun, "Numerical simulation of supersonic Carman curve bodies with aerospike," *International Journal of Aerospace Engineering*, vol. 2021, Article ID 8821721, 14 pages, 2021.

[21] W. Liu, H. Y. Zhao, and X. L. Yang, "Analysis of dynamic stability and research of passive control method for capsule," *Scientia Sinca*, vol. 40, no. 9, pp. 1156–1164, 2010, (In Chinese).

[22] J. Z. Chen, Z. L. Zhao, C. H. Fan, and Y. Li, "Forced-oscillation dynamic derivative test techniques in 2meter scale high speed wind tunnels," *Acta Aerodynamica Sinica*, vol. 34, no. 5, pp. 598–605, 2016, (In Chinese).

[23] C. J. Su, L. H. Chen, X. L. Yang, and W. Liu, "Numerical investigation of dynamic characteristics of blunt cone in large-amplitude under the conditions of force-pitching vibration," *Journal of Ballistics*, vol. 22, no. 1, pp. 53–56, 2010, (In Chinese).

[24] L. P. Zhang and Z. J. Wang, "A block LU-SGS implicit dual time-stepping algorithm for hybrid dynamic meshes," *Computers & Fluids*, vol. 33, no. 7, pp. 891–916, 2004.

[25] X. H. Chang, L. P. Zhang, and X. He, "Numerical study of the thunniform mode of fish swimming with different Reynolds number and caudal fin shape," *Computers & Fluids*, vol. 68, pp. 54–70, 2012.

[26] T. J. Birch, D. K. Ludlow, and N. Qin, "Towards an efficient, robust and accurate solver for supersonic viscous flows," in *ICAS2000 Congress, Royal Aeronautical Society*, London, 2000.

[27] R. Paciorri, W. Dieudonne, G. Degrez, J. M. Charbonnier, and H. Deconinck, "Exploring the validity of the Spalart-Allmaras turbulence model for hypersonic flows," *Journal of Spacecraft and Rockets*, vol. 35, no. 2, pp. 121–126, 1998.